JOURNAL OF COMPUTATIONAL PHYSICS **143,** 70–89 (1998)
ARTICLE NO. CP985974

A Divide-and-Conquer Implementation of the Discrete Variational DFT Method for Large Molecular and Solid Systems

Oliver Warschkow,* John M. Dyke,*,[1] and Donald E. Ellis†

*Department of Chemistry, University of Southampton, Highfield, Southampton SO17 1BJ, United Kingdom; and †Department of Physics and Astronomy, Northwestern University, Evanston, Illinois 60208
E-mail: jmdyke@soton.ac.uk

Received August 12, 1997; revised February 10, 1998

In this paper a novel density functional theory code is described that implements Yang's divide-and-conquer approach in the framework of the discrete variational method. The primary aim of the software is the rapid computation of approximate electron densities and density of states for a given arrangement of atoms. By using moderately sized grids and compact basis and density fit function sets, a high degree of efficiency is achieved. Through the use of the example of linear alkane chains, it is demonstrated that the performance of the method scales linearly with respect to system size for up to more than 1000 atoms. Details of the implementation are given where emphasis is placed on the approximations made and how linear scaling is achieved. Finally, calculations on some example structures will be presented to survey possible applications of the code.

Key Words: DFT; divide-and-conquer; discrete variational method; linear scaling DFT.

1. INTRODUCTION

Electronic structure calculations from first principles have come a long way over the past 25 years and are now, for small molecules, almost routine. However, for larger molecules of 100 atoms and more, the scaling of cpu-time with respect to system size of $O(N^3)$ and higher makes calculations on such systems prohibitively expensive.

A major breakthrough was achieved when the divide-and-conquer (D&C) philosophy, used in other areas of computational science (e.g., the eigenvalue problem [1]), was applied by Yang [2–6] to density functional theory (DFT). By dividing the system into subsystems for which the Kohn–Sham equations are solved separately, D&C imposes a strict localization

[1] To whom correspondence should be addressed.

0021-9991/98 $25.00

constraint to the problem which formally reduces the $O(N^3)$ scaling associated with the building and diagonalization of the Hamiltonian matrix into $O(N^2)$ and $O(N)$ scaling processes, respectively. By further making use of the short-range nature of the exchange–correlation interaction and the smoothness of the coulomb far-field [7], the Hamiltonian matrix-build can also be made linearly scaling, such that an overall $O(N)$ scaling DFT scheme results.

Yang's practical implementation of this method [2, 3] employs the DMol approach [8] to solve the subsystem Kohn–Sham equations. Implementations of D&C based on Gaussian-type orbitals (GTOs) with their advantage of largely analytical integrability are under development [9, 10]. Significant progress has also been reported for strategies that are not based on D&C but use other means of imposing localization [11–16]. Recently, work has been published which concentrates on making the evaluation of the Hamiltonian matrix elements a linearly scaling process with the notion that this is the time-critical part in GTO-based Hartree–Fock and DFT schemes for moderately large system sizes [17–23].

These implementations offer the prospect that accurate single point energy calculations and possibly geometry optimizations using energy gradients will be possible for large molecules in much the same way as they are at present for small molecules. However, in order to obtain reliable energies and gradients, it is paramount that errors arising from approximations introduced (e.g., in the evaluation of the coulomb potential or in the use of numerical integration schemes) are reduced to a minimum.

In contrast, if one were to put aside total energies and their gradients as targets of a calculation, it has been shown that sufficiently accurate electron densities and density of states (DOS) for direct analysis can be obtained efficiently using the discrete variational method (DVM) [24–26], namely numerical integration of the Kohn–Sham equations over moderately sized grids. Such densities (and quantities derived from them) are of course exceedingly useful in themselves: Concepts introduced and discussed for example by Bader, Parr, and others [27–30] can be used to assess properties such as the reactivity of the system under consideration.

The implementation of the D&C DFT approach presented in this work follows the spirit of DVM in that approximate electron densities for a given system are made the primary objective of a calculation. The accuracy required for the calculation of molecular energies will be sacrificed for efficiency and a comparably aggressive level of approximation will be used while trying to retain meaningful densities and DOSs for direct analysis.

In particular, (1) compact numerical orbital basis sets will be used, (2) a simple hierachical model of approximations (controlled by user-defined distance cutoffs) makes the evaluation of the (Kohn–Sham) effective potential a linearly scaling process, (3) integration is performed over comparatively coarse numerical grids ($<$1000 points/atom), and (4) compact density fit basis sets (generally of s-type functions only) are employed. It will be demonstrated that such an approach will allow first principles electronic structure calculations on systems that would otherwise not be accessible by the more accurate approaches listed above.

The following discussion begins with a summary of Yang's D&C method, which also serves the purpose of introducing the terminology used in subsequent sections. Then, the implementation of this method in the framework of the discrete variational method will be introduced. Finally, the performance characteristics of this implementation will be demonstrated using a variety of example systems, among them a linear alkane of 3002 atoms and a protein of 845 atoms.

2. BACKGROUND

In Kohn–Sham density functional theory [30, 31], the electron density is obtained by solving the one-particle eigenvalue problem in the effective potential

$$V_{KS}[\rho] = V_{nucl} + V_{coul}[\rho] + V_{XC}[\rho] \tag{1}$$

consisting of nuclear, coulombic, and exchange–correlation contributions, respectively. Using an orbital basis set $\{\chi_\mu\}$, the density is usually obtained in the form

$$\rho = \sum_\mu \sum_\nu \rho_{\mu\nu} \chi_\mu \chi_\nu, \tag{2}$$

where $\rho_{\mu\nu}$ is the density matrix. In practice, for large systems, the computation and general handling of the density matrix using established methods become prohibitively expensive. However, this problem can be neatly and efficiently overcome by using Yang's divide-and-conquer DFT [2–6]. The essentials of D&C will be summarized in this section but slightly reformulated to emphasize the role of what will be referred to in the following as the "density function" of an atom A, $\rho_A(r; E)$:

$$\rho_A(r; E) = \hat{P}_A \, \rho(r; E) = \sum_i F(E - \epsilon_i) \hat{P}_A |\psi_i|^2. \tag{3}$$

In this equation, F is the Fermi function at finite temperature; ϵ_i and ψ_i are orbital energies and wavefunctions, respectively; and $\hat{P}_A$ is a suitable operator (see below) that partitions densities into atomic contributions. Thus, for a given, yet to be determined, Fermi energy E_f, $\rho_A(r; E_f)$ represents the density associated with atom A. The total density of the system is then of course the superposition of the densities associated with all atoms:

$$\rho(r; E_f) = \sum_A \rho_A(r; E_f). \tag{4}$$

The divide-and-conquer method is based on the principle that $\rho_A(r; E)$, as it would be obtained for a particular atom A in a Kohn–Sham-type calculation on the entire system, is well approximated by the atomic density function $\rho_A^\alpha(r; E)$ obtained for the same atom in a calculation carried out localized to a small "quantum" fragment α of atoms (in the following text a superscripted α signifies a quantity associated with a fragment),

$$\rho_A(r; E) \simeq \rho_A^\alpha(r; E), \tag{5}$$

where

$$\rho_A^\alpha(r; E) = \hat{P}_A \rho^\alpha(r; E) = \sum_i F(E - \epsilon_i) \hat{P}_A \left|\psi_i^\alpha\right|^2. \tag{6}$$

Localization in this context means that the Kohn–Sham equations (for the potential given in Eq. (1)) are solved using orbital basis functions sited only on a small number of atoms (a fragment) including atom A and other nearby (buffer [3]) atoms, which yields orbitals ψ_i^α and densities ρ^α being limited in spatial extent to the fragment. In doing this, the (formally) $O(N^3)$ computational effort in diagonalizing the Hamiltonian matrix of the entire system is avoided and replaced with the linear scaling problem of diagonalizing N small fragment matrices.

Atom A will be referred to in the following as the "reference atom" of the fragment since its density function is used to approximate the density function of a system atom. The accuracy of this approximation is determined solely by the size of the fragment, i.e., the number of buffer atoms used to shield the reference atoms from the surface of the fragment. Of course, more than one atom in a fragment can serve as a reference for a density function.

With atomic density functions obtained in this way for all atoms and with a known electron count N_e, the Fermi level E_f can be computed by requiring that the total density (Eq. (4)) integrates to N_e; thus

$$\sum_A \langle \rho_A(r, E_f) \rangle = \sum_A N_A(E_f) = N_e, \tag{7}$$

where N_A is the number of electrons associated with atom A and the square brackets $\langle \cdots \rangle$ imply integration over all space. Knowing the Fermi level, the electron density ρ is obtained by Eq. (4) and a new effective potential V_{KS} (Eq. (1)) for the system can be constructed; this completes the SCF cycle in a divide-and-conquer DFT calculation.

It is instructive to remember that earlier embedded cluster schemes are based on this very same principle of "localization." In many applications of these methods, the atoms of a solid are described using a single, suitably chosen fragment of the solid (the cluster) for which solid-like densities are obtained in the inside. The crystal potential in which the cluster equations are solved is constructed using the densities of atoms within the cluster as a reference (e.g., Ref. [32]). Thus one can think of Yang's D&C approach as a very elegant extension of the embedded cluster scheme to obtain the density functions for the atoms of a large system, by simply using several (not just one) small clusters/fragments as sources of reference for atomic densities.

A short comment on the partition operator $\hat{P}_A$ used in Eq. (3) is in order. Two forms have been introduced: In the original formulation of D&C [2], a smooth partition function $P_A(r)$ has been used, while in the later "density matrix" D&C [6], partitioning was based on a Mulliken-type scheme; the latter will be used here. In principle, the partitioning is arbitrary and can take any form (as long as $\sum_A \hat{P}_A = 1$). However, the choice affects the quality of the localizing approximation in Eq. (5) when fragment sizes are smaller.

With the principles of Yang's D&C DFT summarized, the practicalities of an implementation using the discrete variational method can be described.

3. IMPLEMENTATION IN THE FRAMEWORK OF THE DVM

In this implementation of divide-and-conquer DFT, calculations on individual fragments are performed using the discrete variational method [24–26]; this part of the present code thus resembles the original DVM code and the core of the now highly sophisticated Amsterdam Density Functional (ADF) package [33]. Briefly, all integrations are performed numerically over a grid of suitably chosen integration points. The densities obtained are least squares fitted to a set of density fit functions which allows a rapid evaluation of the coulombic potential [34].

In the following sections, those parts of the DVM that have to be modified to be suitable and efficient in a D&C calculation on a large system are described. In particular, the efficient construction of the effective Kohn–Sham potential at fragment integration points and the density fitting procedure will be discussed.

3.1. *Representation of the Density*

First, a suitable representation for the electron density of the entire system is required. In the original DVM two types of representations are used—first, a density matrix representation (Eq. (2)) via the orbital basis set and second, a linear expansion in terms of a set of density (fit) functions $\{f_{Ai}\}$ centered on all atoms A [34],

$$\tilde{\rho} = \sum_A \sum_i a_{Ai} f_{Ai}. \tag{8}$$

As discussed before, the density matrix representation is cumbersome for large systems and is not really necessary as will become clear later. The density of the entire system will therefore be represented in the form of Eq. (8) only; this shifts the objective of the calculation toward the determination of the expansion coefficients $\{a_{Ai}\}$. In the following text, symbols for densities in the fit function representation will carry a tilde (e.g., $\tilde{\rho}$) to distinguish them from other forms.

The advantage of having the density in the form of Eq. (8) is that the coulomb potential is straightforwardly accessible using the coulomb potentials of fit functions $\{V_{coul}[f_{Ai}]\}$ [34]:

$$V_{coul}[\tilde{\rho}] = \sum_A \sum_i a_{Ai} V_{coul}[f_{Ai}]. \tag{9}$$

The coulomb potentials of fit functions are in turn easily computed using one-dimensional integration [34].

Also it should be noted that in this form, a natural partitioning of the density (and its coulomb potential) into atomic contributions ($\tilde{\rho}_A$ and $V_{coul}[\tilde{\rho}_A]$) is achieved by assigning to an atom the portion that is described by the fit functions located on it:

$$\tilde{\rho}_A = \sum_i a_{Ai} f_{Ai} \qquad V_{coul}[\tilde{\rho}_A] = \sum_i a_{Ai} V_{coul}[f_{Ai}]. \tag{10}$$

Through the use of a suitable integration over the atomic densities, partial charges (Q_A) and higher multipolar moments can be obtained for all atoms. It should be realized that the number of electrons ($\tilde{N}_A = \langle \tilde{\rho}_A \rangle$) assigned to an atom in this way is generally not identical to that assigned to it as part of the D&C approach ($N_A(E_F)$ in Eq. (7)). The equality of these two charges will become an important constraint later in this discussion.

3.2. *Evaluation of the Fragment's Kohn–Sham Potential*

The electron density of the system gives rise to an effective (Kohn–Sham) potential V_{KS} (Eq. (1)) which has to be evaluated for all fragments employed. However, with the density and its coulomb potential in the form of Eqs. (8) and (9), this is still an $O(N^2)$ process (the underlying interactions are pairwise) and simplifications are required to make the computation of V_{KS} efficient and more favorably scaling with system size.

The evaluation of the Coulomb potential poses particular problems due to its long-range nature, and (linear scaling) techniques for its accurate evaluation are currently intensely pursued [7, 17].

In the present method, a comparatively simple (and certainly less accurate) scheme of approximations depending on the separation of interacting atoms is adopted. However, it is felt that such an approach is more consistent with the level of approximation made elsewhere in this implementation (e.g., grid error, basis, and fit set incompleteness).

A series of truncation radii (R_F, $R_D < R_P$), defined in the input of the code, partition for each fragment the atoms of the system into four sets (fragment atoms $\{F\}$, diffuse atoms $\{D\}$, point atoms $\{P\}$, and "leftovers" $\{M\}$—which in the following text are referred to as multipolar atoms). Increasing levels of approximation are used to evaluate the Kohn–Sham potential V_{KS} created by the atoms in these sets which are subsequently combined to give the total potential

$$V_{KS}(r) = V_{\{D,F\}}(r) + V_{\{P\}}(r) + V_{\{M\}}(r). \tag{11}$$

Fragment atoms $\{F\}$. As discussed before, fragment atoms are those atoms that carry basis functions in a localized quantum calculation. The fragment initially contains only the atoms that serve as reference atoms for the construction of the system density and is extended by all atoms that are within a distance of R_F to any of the reference atoms. Yang [3] refers to the atoms added in this way as "buffer atoms."

Diffuse atoms $\{D\}$. All atoms that are within a distance of R_D of any fragment atom form the set of diffuse atoms $\{D\}$. The atoms of the fragment and diffuse set are represented as containing a nuclear point charge surrounded by a diffuse cloud of electrons. This electron density gives rise to an exchange/correlation potential. Hence, the effective potential (Eq. (1)) due to this subset of atoms is evaluated exactly. An additional approximate potential is introduced to simulate the effect of orbital orthogonality between fragment atoms and surrounding density. In principle, this can be achieved in a simple way by truncating the Kohn–Sham potential within a preset radius of the "embedding" diffuse atoms to a constant potential close to the Fermi level of the system [35]. Here, the electron densities of the fragment and the diffuse set ($\tilde{\rho}_{\{F\}}$ and $\tilde{\rho}_{\{D\}}$) are used to compute the somewhat more elaborate non-additive kinetic energy potential correction $V_{TF,nadd}[\rho_2, \rho_1]$ introduced by Cortona [36, 37] based on the Thomas–Fermi kinetic energy (TF-KE) functional (see also Ref. [38] and comment [39]).

The full potential due to fragment and diffuse atoms is thus given by

$$V_{\{D,F\}}(r) = \sum_{A\in\{D,F\}} \left[-\frac{Z_A}{|r - r_A|} + V_{coul}[\tilde{\rho}_A]\right] + V_{xc}\left[\tilde{\rho}_{\{D\}} + \tilde{\rho}_{\{F\}}\right] + V_{TF,nadd}\left[\tilde{\rho}_{\{F\}}, \tilde{\rho}_{\{D\}}\right], \tag{12}$$

where

$$V_{TF,nadd}\left[\tilde{\rho}_{\{F\}}, \tilde{\rho}_{\{D\}}\right] = \frac{1}{2}(3\pi^2)^{2/3}\left[\left(\tilde{\rho}_{\{F\}} + \tilde{\rho}_{\{D\}}\right)^{2/3} - \left(\tilde{\rho}_{\{F\}}\right)^{2/3}\right] \tag{13}$$

and

$$\tilde{\rho}_{\{F\}} = \sum_{A\in\{F\}} \tilde{\rho}_A \qquad \tilde{\rho}_{\{D\}} = \sum_{A\in\{D\}} \tilde{\rho}_A. \tag{14}$$

The density and coulomb potential ($\tilde{\rho}_A$, $V_{coul}[\tilde{\rho}_A]$) associated with an atom are given by their expansions (Eq. (10)) into density fit functions and their potentials, respectively.

Point atoms $\{P\}$. Atoms that are at distances between R_D and R_P from any fragment atom are represented as point atoms. In essence, it is assumed that the electron density associated with these atoms does not reach the region of the fragment, which means that the coulomb potential is effectively that of a point multipole. Currently, a further approximation

is made of retaining only the point charge term in the potential, neglecting higher multipoles. The potential is then given by

$$V_{\{P\}}(r) = -\sum_{A\in\{P\}} \frac{Q_A}{|r - r_A|}. \tag{15}$$

Multipolar atoms $\{M\}$. The coulombic potential due to all atoms that are at distances larger than R_P from any fragment atom, and thus not represented in any of the other atom sets, is assumed to be nearly constant and therefore representable using a truncated multipolar expansion around a suitable center r_0 of the fragment:

$$V_{\{M\}}(|r - r_0|, \Omega) = \sum_{lm}^{l_{max}} M_{lm} Y_{lm}(\Omega)|r - r_0|^l. \tag{16}$$

The multipolar moments M_{ml} in this expansion are obtained by summation over the charge weighted contributions of the single atoms. Again, the atoms are assumed to be point charges:

$$M_{ml} = \sum_{A\in\{M\}} Q_A M_{ml,A}. \tag{17}$$

The multipolar moments $M_{ml,A}$ generated by a unit charged atom A around r_0 are dependent only on the relative position of the atom. They are conveniently computed before SCF commences. In the case of a periodic system, the crystal (Madelung) potential is also represented in this form, which results in a set of crystal moments $M^{xtl}_{ml,A}$ for each atom in the asymmetric unit. Currently, moments up to $l_{max} = 2$ are used.

In the practical implementation, various function values at integration points, needed in the evaluation of the effective potential, are computed only once before SCF and stored on disk. This includes the density fit functions f_{Ai} and their coulomb potentials $V_{coul}[f_{Ai}]$, unit point charge potentials (for Eq. (15)) as well as the multipolar potential functions $(Y_{lm}|r - r_0|^l)$ for Eq. (16). With these data readily available from disk, the evaluation of the potential (Eqs. (1) and (11)) in integration points $\{V_{KS}(r_i)\}$ during each SCF cycle proceeds rapidly. Indeed, the subsequent numerical integration of the potential and the symmetrized basis functions (also read from disk) over the grid $\{r_i, w_i\}$ to form the Hamiltonian

$$\begin{aligned} H^{\alpha}_{\mu\nu} &= T^{\alpha}_{\mu\nu} + \int dr\, \chi_\mu(r) V_{KS}(r) \chi_\nu(r) \\ &\simeq T^{\alpha}_{\mu\nu} + \sum_i w_i \chi_\mu(r_i) V_{KS}(r_i) \chi_\nu(r_i) \end{aligned} \tag{18}$$

usually dominates this part of the SCF procedure (T^α is the kinetic energy matrix).

Looking at the scaling properties of this part of the method with respect to increasing system size, it should be noted that above a certain critical system size, the number of atoms located within any of the three cutoff radii (i.e., atom sets $\{F\}$, $\{D\}$, $\{P\}$) remains constant. Hence the number of terms to be evaluated for these atoms is constant and the computational effort of calculating these terms for all fragments becomes linearly scaling. The only exceptions to this are the terms associated with the "multipolar atoms" outside the outermost cutoff R_P (atom set $\{M\}$) whose number increases with system size; thus the evaluation of this part of the potential ($V_{\{M\}}$, specifically the sum in Eq. (17)) for all fragments

scales quadratically. In principle, this part of the potential can also be made linearly scaling using a fast multipole approach [7]. However, since the multipolar part of the potential is calculated rapidly in comparison with the other parts, its quadratic scaling is not expected to become significant for practical system sizes (see performance discussion below).

3.3. *Density Fitting*

With the Fermi level E_f computed for the system (Eq. (7)), the density for the entire system is in principle available via the density functions defined in Eqs. (3) and (4), which would eventually yield a density matrix representation (Eq. (2)) of the system density [6]. The density expansion coefficients $\{a_{Ai}\}$ of Eq. (8) could then be obtained by least squares fitting, as is standard practice in the standard DVM [34]. However, such a least squares fitting approach would result in an $O(N^3)$ scaling process (since it requires the inversion of a $O(N)$ sized matrix) and a linear scaling alternative is required. Using a localization ansatz similar to the one used in Yang's D&C, such an alternative has been described by St. Amant and co-workers [9, 10] for the LCGTO-DFT method [40, 41] and the approach in the following can to some extent be considered an adaptation to the DVM. However, unlike St. Amant's fitting procedure, the present method will not require a density matrix representation (Eq. (2)) of the entire system density. Instead, fitting will be based only on the densities ρ^α obtained for all the fragments as a result of the D&C method.

This begins with Eq. (8) being least squares fitted to fragment densities,

$$\rho^\alpha = \sum_i f\left(\epsilon_i^\alpha - E_f\right)\left|\psi_i^\alpha\right|^2, \tag{19}$$

giving rise to a complete set of fit expansion coefficients $\{a_{Ai}^\alpha\}$ for each fragment. Then, the expansion coefficients found in this way for the reference atoms of a fragment are taken as approximations for those obtained if the density fit were performed on a globally represented density. Thus, the approximation Eq. (5) translates into

$$a_{Ai} \simeq a_{Ai}^\alpha. \tag{20}$$

In this way expansion coefficients $\{a_{Ai}\}$ for all atoms of the system can be obtained by referencing appropriate atoms in the set of fragments.

Because fragment densities ρ^α are localized to small regions of the system only fit functions located on atoms that are either part of or close to the fragment will be significantly involved in the expansion. Since one is interested only in the expansion coefficients obtained for reference atoms in the inside of the fragment, it is a reasonable step to truncate the fit function representation of ρ^α to involve functions located on fragment atoms only:

$$\tilde{\rho}^\alpha = \sum_{A\in\{F\}} \sum_i a_{Ai}^\alpha f_{Ai}. \tag{21}$$

This truncation results in the number of fit functions involved in a fragment least squares fit to be (asymptotically) constant with system size, which means that the density fit for all fragments will be a linearly scaling process.

An important constraint in the fragment fitting procedure is the conservation of charge for the entire system. This can be conveniently achieved by requiring that the fitted density associated with a reference atom A ($\tilde{\rho}_A$, Eq. (10)) integrates to the same number of electrons that has been assigned to it earlier in Eq. (7)—namely $N_A(E_f)$, the integrated atomic density

function at the Fermi level E_f:

$$\left\langle \tilde{\rho}_A^{\alpha} \right\rangle = \sum_i a_{Ai}^{\alpha} \langle f_{Ai} \rangle = N_A \qquad \forall A \in \{R\}. \tag{22}$$

This is achieved by augmenting the least squares fit of Eq. (21) to Eq. (19) for a fragment by a constraint of the form Eq. (22) for each reference atom defined by it. Non-reference (buffer) atoms of a fragment are not constrained. The Lagrangian of the least squares fit is then given by

$$L = \langle (\rho^{\alpha} - \tilde{\rho}^{\alpha})^2 \rangle - \sum_{A \in \{R\}} \lambda_A \left(\left\langle \tilde{\rho}_A^{\alpha} \right\rangle - N_A \right). \tag{23}$$

Minimization of L for all fragments α, which equates to solving a set of linear equations, yields the expansion coefficients $\{a_{Ai}^{\alpha}\}$ which are used in conjunction with approximation Eq. (20) to construct the fit function representation of the system density (Eq. (8)).

During the SCF procedure, an updating strategy is required to ensure convergence of the electron density (i.e., coefficients $\{a_{Ai}^{\alpha}\}$) to a stationary solution. In this implementation, the convergence is reached when changes in the density expansion coefficients $\{a_{Ai}\}$ are below a preset threshold. To accelerate convergence, Pulay's DIIS [42, 43] extrapolation procedure is applied to generate updated coefficients for the next cycle.

With this, the core of the present "divide-and-conquer" implementation of the discrete variational method has been described. In the following section, some of the more practical aspects are discussed.

3.4. *Use of Symmetry*

In this implementation of the divide-and-conquer approach, the use of symmetry sets in at two different levels. First, symmetry in each fragment is used to factorize the Kohn–Sham matrix equation and to generally reduce the work load as is standard practice in most quantum chemical codes. More importantly, symmetries in the global system can be used to much advantage. Because the system density is required to be totally symmetric, the atomic density of only one atom in a set of symmetry equivalent atoms needs to be computed in a fragment calculation [5]. The transfer of these densities to symmetry-related sites typically requires a rotation of the local coordinate system.

To use this symmetry in practice, the only information required in the input is to assign all atoms to sets of equivalent atoms (referred to as a potential type [32]). The relative orientation of two atoms in such a set can then be worked out using the position and potential type of their respective three nearest (nonplanar) neighbors. The specification of the point or space group of the system and its symmetry operations is not required. This greatly simplifies calculations on symmetric systems with or without periodicity; a particular advantage is that special symmetries (e.g., helical geometries) can be used just as easily as any other symmetry.

3.5. *Basis Sets*

One of the advantages of all-numerical integration schemes is that no restrictions on the type and shape of basis functions are imposed. Highly compact, yet accurate orbital basis sets are obtained if they are based on wavefunctions from numerical atomic density functional calculations [34]. The functions used in the following calculations are generally of valence double numerical (VDN) type. For core basis functions, the core atomic functions of the

atom (in its reference state) are used, and for valence basis functions, atomic functions of the atom in two different oxidation states are used. For atoms such as C, N, O, and S in covalent environments, these oxidation states are the single positive and negative ions, respectively. For atoms in ionic environments, e.g., Si in silicates, the basis set is constructed from atomic functions of the fully (Si^{4+}) and partially (Si^{2+}) ionic atom. Density fit sets are also based on atomic orbital calculations. Typically, density fit functions are obtained by taking spherically averaged and squared orbital basis functions for the radial part augmented with the appropriate spherical harmonic for the angular part.

4. PERFORMANCE

A series of calculations were carried out to establish various performance characteristics of the code. The example of a linear alkane chain is used to demonstrate that cpu time and disk usage do indeed scale linearly with system size over a wide range. The effect of increasing fragment size on computed properties is studied for a solid silicate structure (Annite). Finally a trial run is presented to compute the electronic structure of the 845 atom protein *Thermotoga maritima* 1 [Fe_4S_4] Ferredoxin [45].

4.1. *Linear Alkane Chains*

To test how the performance of the code scales with system size, a series of *n*-alkanes C_nH_{2n+2} were constructed with n ranging from 2 to 1000. The alkane chains are linearly stretched in space (all CCCC dihedral angles are 180°), with bond lengths $d(\mathrm{CC}) = 1.54$ Å and $d(\mathrm{CH}) = 1.07$ Å and angles $\alpha(\mathrm{CCC}) = 109.5°$. Although these structures belong to the C_{2h} or C_{2v} point groups (depending on whether n is even or odd), no use of this symmetry is made in the following timing calculations to make them representative of similar but less symmetric systems.

A valence double numerical basis set is used with carbon 1*s* orbitals kept frozen during the SCF procedure. The density fit set consists of *s*-functions only, based on spherically averaged squares of selected basis functions. This results in four and two fit functions on C and H atoms, respectively. The alkanes C_nH_{2n+2} are divided into n fragments, where each fragment serves as a reference for one carbon atom and the two hydrogen atoms attached to it. In addition to these reference atoms, the fragment includes the nearest two methylene groups in each direction as buffer atoms ($R_F \approx 6$ bohrs). The other truncation radii R_D and R_P (defined in the text above) were set to 10 and 20 bohrs, respectively. With these parameters, a typical fragment in the center of an alkane contains 15 fragment atoms, 24 diffuse atoms, and 24 point ions. The other atoms of the system are represented using the multipolar expansion (Eq. (16)) where an upper limit $l_{max} = 2$ has been adopted. Here 9989 integration points are used to evaluate the Hamiltonian matrix elements of this fragment.

The timing calculations were performed in single-processor dedicated mode on an SGI Power Challenge (75-MHz R8000 processors) computer. Generally, the calculations were not run to full convergence and were stopped after the time was taken for the first SCF cycle. However, to confirm that the system does converge, alkanes with $n = 100$, 500 and 1000 were run to full self-consistency ($\mathrm{RMS}(\Delta a_{Ai}) < 10^{-6}$ and $\mathrm{MAX}(\Delta a_{Ai}) < 10^{-3}$). For these examples, no notable effect of system size on the rate of convergence could be detected. The $n = 1000$ alkane, for example, met the convergence criterion after 11 cycles.

Selected CPU times and disk space requirements are displayed in Table 1. Average times per fragment are given in parentheses. The same data are displayed graphically in Fig. 1.

TABLE 1
CPU Times for (pre-SCF) Setup and One SCF Cycle as well as Disk Space Required for a Series of Linear Alkanes C_nH_{2n+2} Divided into *n* Fragments

n	Atoms	Setup/s	SCF-cycle/s	Disk/MB
2	8	19 (10)	3 (2)	5 (3)
5	17	123 (25)	19 (4)	35 (7)
10	32	330 (33)	50 (5)	106 (11)
20	62	755 (38)	114 (5.7)	266 (13)
30	92	1178 (39)	180 (6.0)	422 (14)
50	152	2024 (41)	310 (6.2)	736 (15)
75	227	3082 (41)	473 (6.3)	1127 (15)
100	302	4148 (41)	637 (6.4)	1520 (15)
200	602	8424 (42)	1293 (6.5)	3090 (15)
300	902	12770 (43)	1975 (6.6)	4665 (16)
400	1202	17157 (43)	2660 (6.6)	6248 (16)
500	1502	21615 (43)	3354 (6.7)	7831 (16)
750	2252	33179 (44)	5145 (6.9)	11812 (16)
1000	3002	45363 (45)	7005 (7.0)	15817 (16)

Note. Quantities in parentheses refer to average amounts per fragment. The cpu utilization (wall clock time over cpu time) was in all cases above 98% for the setup and above 87% for SCF. The remaining percentage is largely associated with the time spent on disk IO.

As can be seen in Fig. 1A, the time and disk space requirements show linear scaling to a very good degree. The data points bend slightly away from the dotted line at higher *n* but this is far from showing a parabolic increase. This becomes clearer in the double logarithmic plot (Fig. 1B), where all the data points are located very close to a line of slope 1, signifying that the scaling is predominantly linear. Following the fitted curves in this figure beyond the range of data points, a rough prediction for the crossover from linear (slope 1) to quadratic (slope 2) scaling can be made. The solid curve which contains the quadratic term begins to bend over to a slope 2 line. This transition starts to set in significantly at $n = 5 \times 10^3$ and is fully realized at $n = 10^5$. It is noted that the effective scaling at the largest data point in this example, $n = 1000$ (3002 atoms), as estimated from the slope of the fitted curve in the double logarithmic plot, is below 1.1, thus clearly within a predominantly linear regime.

Two comments about these calculations are in order.

(1) The scaling calculations were performed on an essentially linear system as opposed to a more bulky, three-dimensional structure. Obviously, calculations on such a system would require larger computing times since more atoms would fall within any of the potential cutoff radii. But as outlined above, only the "multipolar" atoms located outside the outermost cutoff (R_P) show quadratic scaling. Therefore calculations on three-dimensional structures are expected to show similar $O(N)$ scaling. On the other hand linear structures maximize the proportion of "multipolar atoms"; hence the onset of quadratic scaling should occur earlier (lower N) as would otherwise be the case for bulkier structures.

(2) The division of the alkanes into *n* subsystems is not the most time-efficient choice of fragmentation. Significant improvements in computing time can be achieved by using fewer fragments, each describing more than one methylene group. With the choice of cutoff parameters used, the optimum fragmentation pattern was found to be three methylene groups

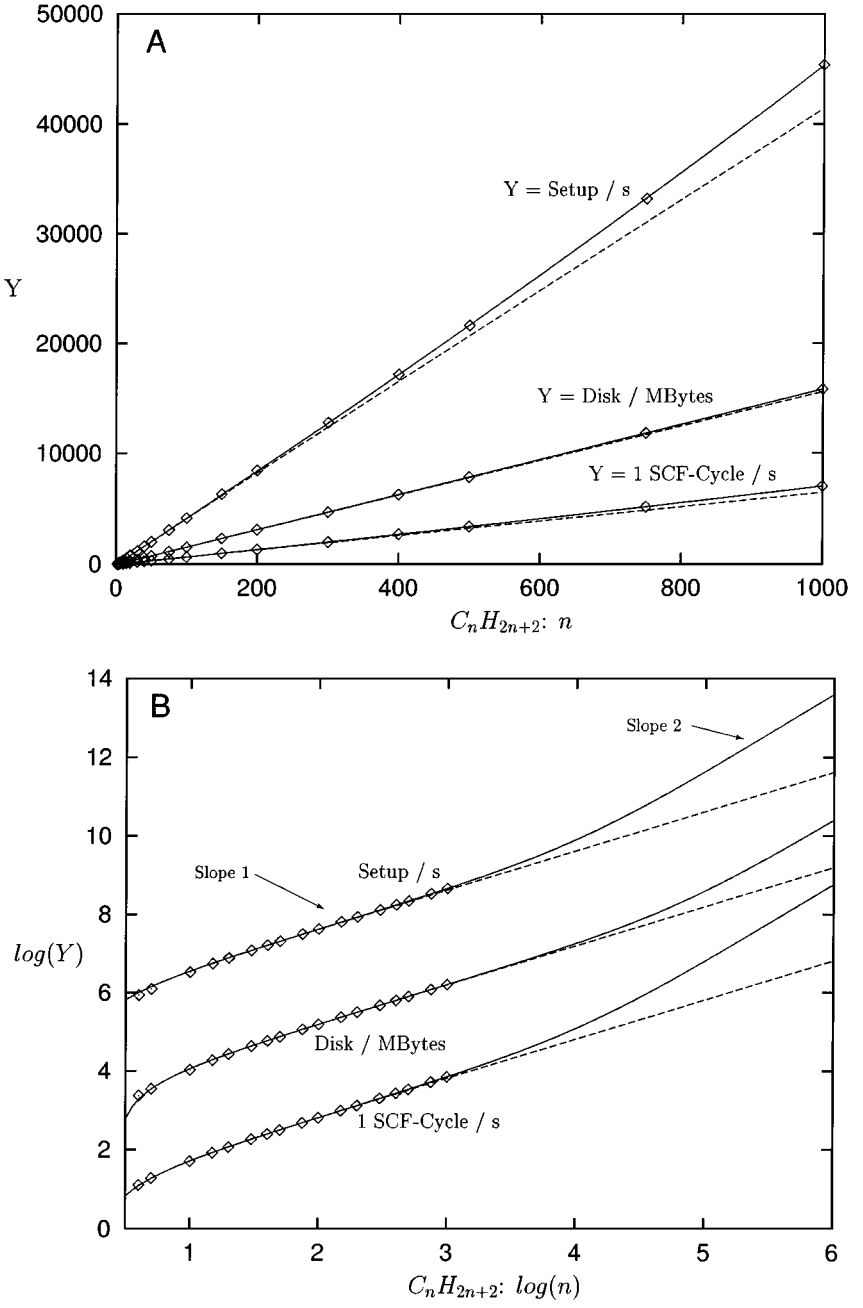

FIG. 1. (A) CPU-time in seconds for one SCF cycle and pre-SCF setup as well as disk space in megabytes required for a series of linear alkanes C_nH_{2n+2}. In all plots, the measured data points are represented as boxes. The solid curve is obtained by fitting the data points $\{Y, n\}$ to an expression of the form $Y = a + bn + cn^2$. In order to show the extent of quadratically scaling terms, the same function, with the quadratic term omitted, is displayed as a dotted line. (B) The same data in double logarithmic form. In such a plot, the slope of the data corresponds to the effective order of scaling. For clarity, the data for setup and disk usage in this plot have been vertically shifted by two and four units, respectively.

per fragment, resulting in $n/3$ fragments. In practice the optimum partitioning will be highly dependent on the system at hand and the choice of cutoff parameters.

4.2. *Annite Layered Silicate*

Calculations on this material using a DVM single cluster model have been performed recently by one of the authors with the objective of calculating Moessbauer hyperfine parameters [44]. Here, the same material is taken as a (moderately sized) example to study the effect of fragment size (effectively controlled by cutoff parameter R_F) on computed properties.

The chemical composition of ideal annite is $KFe_3(AlSi_3)O_{10}(OH)_2$, with two formula units in the crystal unit cell (spacegroup $C2/m$). Briefly, the structure consists of layers made up of two opposing tetrahedral sheets of silicon/aluminium oxide attached to a sheet of octahedrally coordinated iron atoms. Potassium atoms are located between these layers to ensure charge neutrality [44].

Of the 44 atoms in the unit cell, 24 atoms are symmetry unique which, in this calculation, are described using 22 fragments; two types of hydrogen atoms are in each case described in the same fragment as the nearest oxygen atom. Three calculations (referred to as Models I, II, and III) were performed, with atoms added as buffer atoms to fragments if they are within a distance R_F of 6.0, 7.5, and 9.0 bohrs, respectively, to any reference atom of the fragment. The truncation radii adopted, result, for example, in iron atom types being described by

$$\begin{aligned} &Fe_1O_4(OH)_2Fe_6 && \text{(15 atoms)}\\ &Fe_1O_4(OH)_2Fe_6O_2Si_4O_2O_4 && \text{(27 atoms)}\\ &Fe_1O_4(OH)_2Fe_6O_2Si_4(OH)_2O_4O_4(Si,\,Al)_4O_4 && \text{(41 atoms)} \end{aligned}$$

fragments, respectively (Fig. 2). Similar-sized fragments describe the other atom types. The cutoff parameters R_D and R_P were set to 10 and 14 bohrs, respectively. Since these cutoff distances are measured from any of the fragment atoms, the boundaries described by them move in parallel with the fragment's surface away from the reference atoms with increasing fragment size; thus the effect of approximations to the effective potential (Eq. (11)) is also reduced.

Calculations were performed using local spin density theory (LSDA) where ferromagnetic alignment of Fe magnetic moments has been assumed. The basis set used is of a valence double numerical type, with the frozen core approximation used for atomic orbitals up to

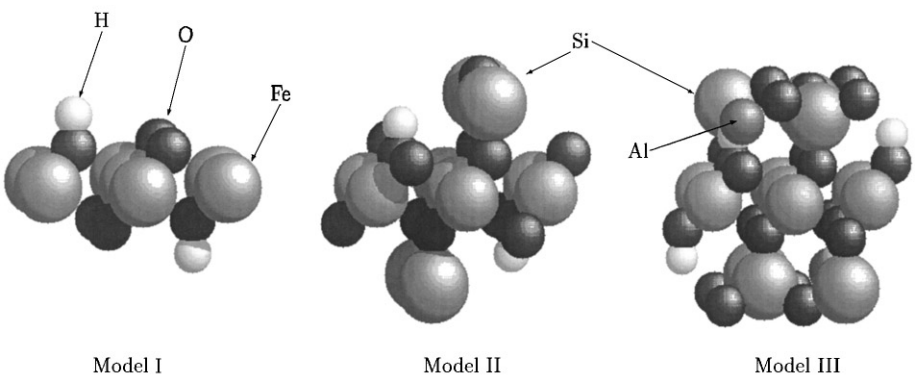

FIG. 2. Fragments used to describe iron atom types in three D&C calculations (Models I to III) on Annite. These fragments were formed by adding to the iron ("reference") atom in the center all atoms within a distance of $R_F = 6.0$, 7.5, and 9.0 bohrs, respectively.

K-2p, Fe-3s, Si-1s, Al-1s, O-1s. Again, only spherically symmetric density fit functions are used.

The total density of states (TDOS) and the iron weighted partial density of states (PDOS) obtained in the three calculations are compared in Fig. 3. The energy ranges shown are

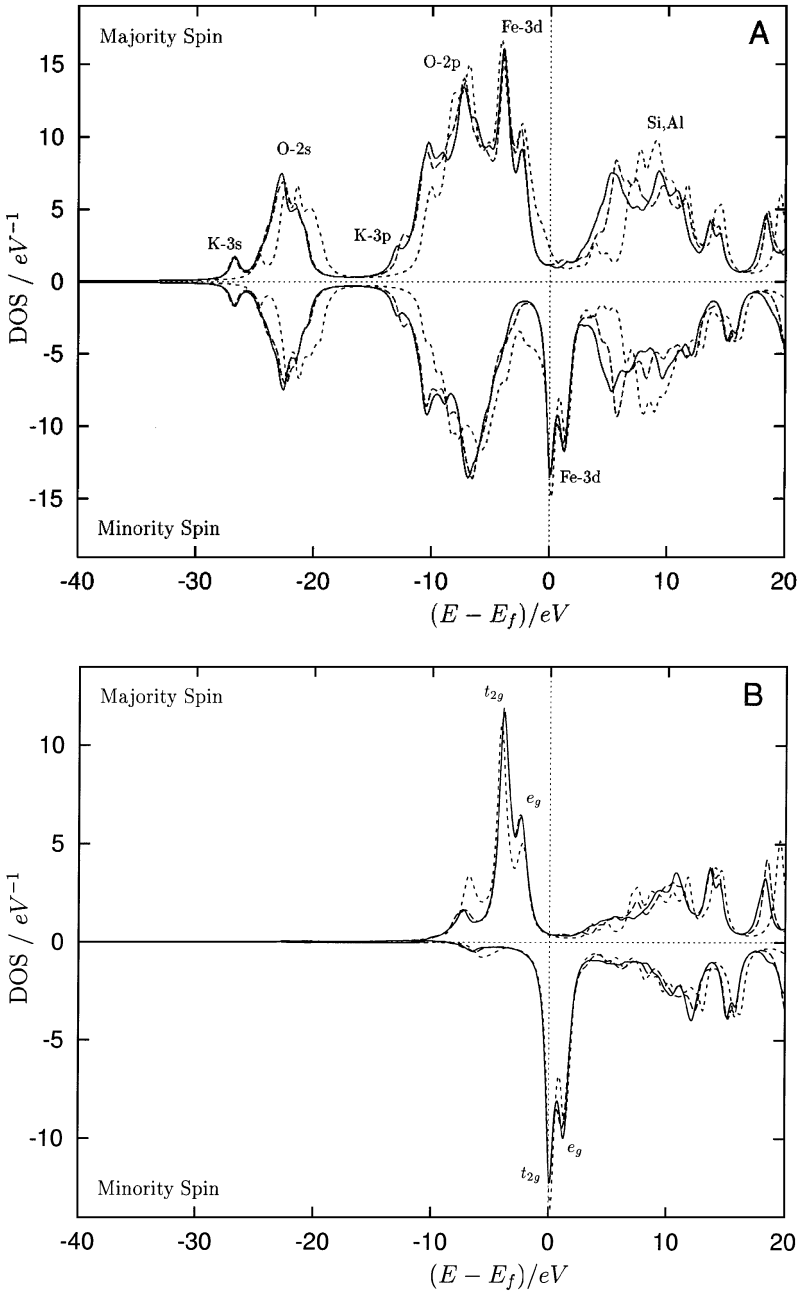

FIG. 3. Comparison of the density of states (DOS) for the layered silicate Annite was obtained using three different fragment sizes (Model I: short dashed line; Model II: long dashed line; Model III: solid line; see text). (A) Total density of states (TDOS); (B) iron partial density of states (PDOS). Energies are relative to the respective Fermi level E_f. In the convolution, Lorentzian distributions of width 0.4 eV have been used.

relative to the computed Fermi level (E_f) of -4.91, -3.67, and -3.53 eV for Models I, II, and III, respectively.

Qualitatively, the DOS is characterized by iron states around the Fermi level, as can be seen from the Fe-PDOS curves. The double peak structure in both spin components of the iron PDOS is caused by the crystal field splitting of iron d-states into states of local symmetry t_{2g} and e_g in the (near-) octahedral crystal field. The DOS structure toward lower energies is mainly of oxygen $2p$ (-10 to -5 eV) and oxygen $2s$ (-25 to -20 eV) character. Potassium $3p$ and $3s$ states are overlapped with the low-energy part of the respective oxygen bands. Unoccupied silicon and aluminum $3s$ as well as iron $4s$ and $4p$ states produce the band with an onset at $+5$ eV.

Comparison of the DOS diagrams obtained for the three models shows them to be very similar in many aspects. Model II and III are nearly indistinguishable for occupied bands, suggesting that the DOS has converged with respect to fragment size. However, even for the smaller Model I, the overall appearence of the bands compares well and even some of the more detailed peak structure of the larger models is nicely reproduced. The most notable difference is an apparent shift of the DOS of Model I by about 1 eV to higher energies relative to Model II and III, with the exception of the iron states which are not shifted. This is probably largely due to the shift in the Fermi level between models I and II. The Fermi level itself is determined by the positioning of the iron states, so that the shift in the DOS diagram can be attributed to an increased energy of the iron states in models II and III as a result of using larger fragments.

In Fig. 4, an electron density contour map calculated for Model III is displayed, centered around one of the iron sites. With its d-band located at the Fermi level, the density around iron atoms should be most sensitive to fragment size effects. To illustrate the extent of these changes, a density difference map between Model I and Model III densities is also presented in the same figure. Comparison of the magnitudes of the contours in the two plots shows that the effect of increased cluster size on the crystal density is very small indeed. The difference between densities of Models II and III, which is not shown in Fig. 4, is even smaller.

In conclusion, the densities and DOS diagrams obtained for Annite in three calculations using different fragment sizes are in good agreement with each other; good convergence with respect to increasing fragment size has been reached. As far as these two particular properties are concerned there seems not to be much advantage of increasing fragment sizes beyond Model II.

4.3. *Example 2: Protein 1 [Fe_4S_4] Ferredoxin*

This protein structure was chosen as an example of a large molecular system. The objective of this example is to show that a DFT calculation on a system of this size can be performed using the present method.

The atomic structure used in this work was obtained from the Brookhaven Protein Database under the entry 1ROF (Structure 1) and is based on solution-NMR data [45]. This protein is a small iron–sulfur electron carrier of the bacterial species *Thermotoga maritima*. It contains 845 atoms in 60 residues and includes a Fe_4S_4 cluster which is coordinated by four cystine sulfide groups. By changing its oxidation state, this cluster is generally believed to be the primary carrier site for electrons. The structure used is that of the fully oxidized form of Ferredoxin with formal Fe_4S_4 cluster charge of $+3$ [45].

For the calculation, the protein was divided into 260 fragments. Potential truncation radii R_F, R_D, and R_P were set to 6.0, 6.0, and 14.0 bohrs, respectively; this means in particular

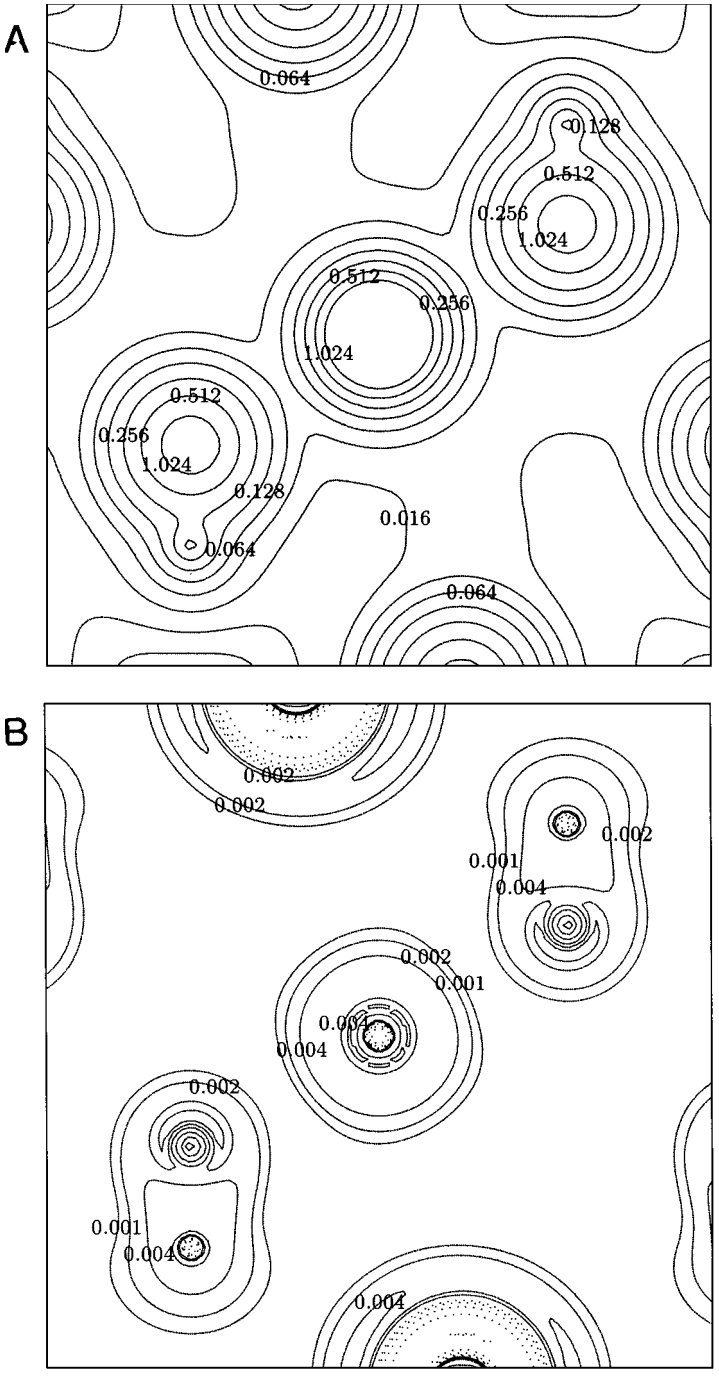

FIG. 4. Comparison of electron densities $\tilde{\rho}$ computed for Annite around an octahedral iron site using different fragment sizes (Models I and III; see text). (A) The electron density map for Model III; (B) the density difference map between Models I and III. Next to the central iron atom two coordinating OH groups are visible. Contour levels are at magnitudes 0.001, 0.002, 0.004, . . . , 1.024 e/a_0^3 with solid and dotted contours for positive and negative values, respectively.

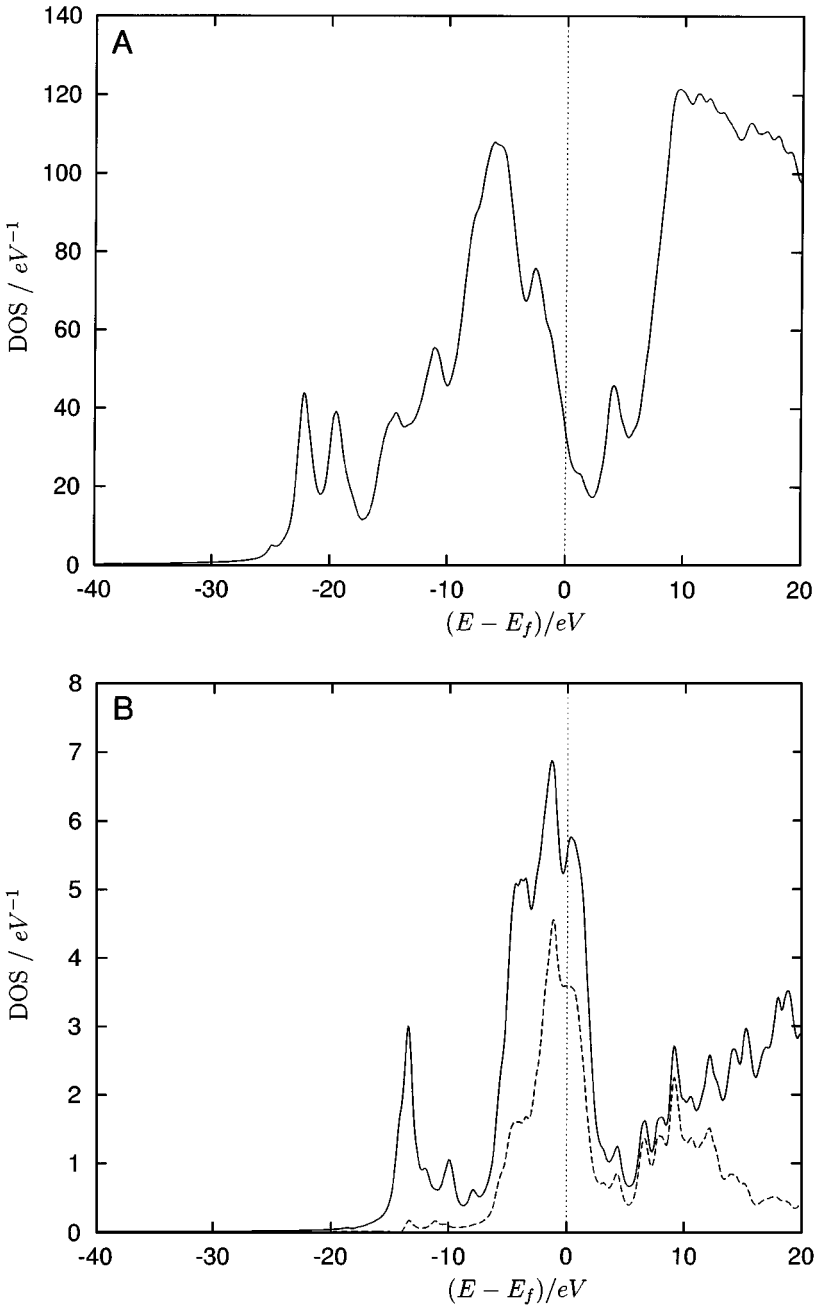

FIG. 5. Electronic density of states computed for a proposed structure of the iron–sulfur protein *Thermotoga maritima* 1 [Fe_4S_4] ferredoxin. (A) The total density of states and (B) the local density of states of the complete iron–sulfur cluster (including four cystein ligand sulfur atoms) overlaid with the contributions of the four iron atoms. Energies are relative to the Fermi level E_f. In the convolution, Lorentzian distributions of width 0.4 eV have been used.

that atoms within a distance R_D less than 6 bohrs to any reference atom were added as buffer atoms to a fragment. As for the alkanes or Annite calculations, a VDN basis set with frozen core approximation and a spherical-only density fit function set were used. Calculations were performed in the spin-restricted (LDA) framework. It should be noted that solvation effects have not been considered in this work.

Upon startup of the calculation, convergence in the electron density proceeded steadily but more slowly than in the case of the alkanes. This was primarily due to charge fluctuations in the iron cluster. Convergence was achieved ($RMS(\Delta a_{Ai}) < 10^{-6}$) after 54 SCF cycles in total. This is in our experience a fairly typical number of cycles for a system that contains transition metals in conjunction with partially filled bands at the Fermi level.

In Fig. 5, the computed total DOS and the Fe_4S_8-weighted DOS (including the ligand sulfur atoms) for this protein are displayed. The total DOS here shows typical features of a protein DOS (compared for instance with the tetrapeptide DOS in Ref. [4]). The iron cluster DOS has its peak directly at the Fermi level, as expected, since these cluster states are the electron carrier states of the protein. Nevertheless, the presence of a solvent will of course have a significant effect on the electronic structure but the discussion of such effects would certainly go beyond the scope of this paper.

5. CONCLUSIONS

The details of a divide-and-conquer implementation of the discrete variational method have been described. By using comparatively coarse numerical integration grids in conjunction with compact orbital and density basis sets, approximate electron densities for large systems are obtained very efficiently and linearly scaling with system size over a wide range. This was demonstrated using linear alkane chains C_nH_{2n+2} for n up to 1000. For this system, the onset of significant quadratical scaling was predicted to be well above several thousand atoms. The convergence of electron densites and densities of states with respect to increasing size of fragments was demonstrated using the example of the layered silicate Annite. Finally, the method was applied to calculate the electronic density of states of an 845 atom protein.

ACKNOWLEDGMENTS

The authors are indebted to J. Terra for providing the unit cell coordinates of Annite. O. W. thanks Magnox Electric/U.K. for a studentship. This research was supported by the EPSRC/U.K. and the U.S. Department of Energy under Grant DE-FG02-84ER45097.

REFERENCES

1. D. C. Sorensen and P. T. P. Tang, On the orthogonality of eigenvectors computed by divide-and-conquer techniques, *SIAM J. Numer. Anal.* **28**, 1752 (1991).
2. W. Yang, Direct calculation of electron density in density-functional theory, *Phys. Rev. Lett.* **66**, 1438 (1991).
3. W. Yang, Direct calculation of electron density in density functional theory: Implementation for benzene and a tetrapeptide, *Phys. Rev. A* **44**, 7823 (1991).
4. C. Lee and W. Yang, The divide-and-conquer density-functional approach: Molecular internal states of rotation and density of states, *J. Chem. Phys.* **96**, 2408 (1992).
5. W. Yang, Electron-density as the basic variable—A divide-and-conquer approach to the ab initio computation of large molecules, *J. Mol. Struct. (Theochem)* **255**, 461 (1992).

6. W. Yang and T. S. Lee, A density-matrix divide-and-conquer approach for electronic structure calculations of large molecules, *J. Chem. Phys.* **103**, 5674 (1995).
7. L. Greengard, Fast algorithms for classical physics, *Science* **265**, 909 (1994).
8. B. Delley, An all-electron numerical method for solving the local density functional for polyatomic molecules, *J. Chem. Phys.* **92**, 508 (1990).
9. R. T. Gallant and A. St-Amant, Linear scaling for the charge density fitting procedure of the linear combination of Gaussian-type orbitals density functional method, *Chem. Phys. Lett.* **256**, 569 (1996).
10. S. K. Goo and A. St-Amant, Using a fitted electronic density to improve the efficiency of a linear combination of Gaussian-type orbitals calculation, *Chem. Phys. Lett.* **264**, 9 (1997).
11. G. Galli and M. Parrinello, Large scale electronic structure calculations, *Phys. Rev. Lett.* **69**, 3547 (1992).
12. X. P. Li, R. W. Nunes, and D. Vanderbilt, Density-matrix electronic-structure method with linear system-size scaling, *Phys. Rev. B* **47**, 10,891 (1993).
13. P. Ordejón, D. A. Drabold, M. P. Grunback, and R. M. Martin, Unconstrained minimization approach for electronic computations that scales linearly with system size, *Phys. Rev. B* **48**, 14,646 (1993).
14. P. Ordejón, D. A. Drabold, R. M. Martin, and M. P. Grumbach, Linear system-size scaling methods for electronic-structure calculations, *Phys. Rev. B* **51**, 1456 (1995).
15. P. Ordejón, E. Artacho, and J. M. Soler, Self-consistent order-N density functional calculations on very large systems, *Phys. Rev. B* **53**, 10,441 (1996).
16. J. M. Millam and G. E. Scuseria, Linear scaling conjugate gradient density matrix search as an alternative to diagonalization for first principles electronic structure calculations, *J. Chem. Phys.* **106**, 5569 (1997).
17. M. C. Strain, G. E. Scuseria, and M. J. Frisch, Achieving linear scaling for the electronic quantum coulomb problem, *Science* **271**, 51 (1996).
18. J. C. Burant and G. E. Scuseria, A linear scaling method for Hartree–Fock exchange calculations of large molecules, *J. Chem. Phys.* **105**, 8969 (1996).
19. C. A. White, B. G. Johnson, P. M. W. Gill, and M. Head-Gordon, Linear scaling density functional calculations via the continuous fast multipole method, *Chem. Phys. Lett.* **253**, 268 (1996).
20. M. Challacombe, E. Schwegler, and J. Almöf, Fast assembly of the Coulomb matrix: A quantum chemical tree code, *J. Chem. Phys.* **104**, 4685 (1996).
21. E. Schwegler, M. Challacombe, and M. Head-Gordon, Linear scaling computation of the Hartree–Fock exchange matrix, *J. Chem. Phys.* **105**, 2726 (1996).
22. E. Schwegler, M. Challacombe and M. Head-Gordon, Linear scaling computation of the Fock matrix. II. Rigorous bounds on exchange integrals and incremental Fock build, *J. Chem. Phys.* **106**, 9708 (1997).
23. M. Challacombe and E. Schwegler, Linear scaling computation of the Fock matrix, *J. Chem. Phys.* **106**, 5526 (1997).
24. D. E. Ellis and G. S. Painter, Discrete variational method for the energy-band problem with general crystal potentials, *Phys. Rev. B* **2**, 2887 (1970).
25. E. J. Baerends, D. E. Ellis, and P. Ros, Self-consistent molecular Hartree–Fock–Slater calculations. I. The computational procedure, *Chem. Phys.* **2**, 41 (1973).
26. A. Rosen, D. E. Ellis, H. Adachi, and F. W. Averill, Calculations of molecular ionization energies using a self-consistent-charge Hartree–Fock–Slater method, *J. Chem. Phys.* **65**, 3629 (1976).
27. R. F. W. Bader, *Atoms in Molecules—A Quantum Theory* (Oxford Univ. Press, Oxford, 1990).
28. W. Kohn, A. D. Becke, and R. G. Parr, Density functional theory of electronic structure, *J. Phys. Chem.* **100**, 12,974 (1996).
29. R. G. Parr and W. Yang, Density functional approach to the frontier-electron theory of chemical reactivity, *J. Am. Chem. Soc.* **106**, 4049 (1984).
30. R. G. Parr and W. Yang, *Density Functional Theory of Atoms and Molecules* (Oxford Univ. Press, Oxford, 1989).
31. W. Kohn and L. J. Sham, Self-consistent equations including exchange and correlation effects, *Phys. Rev. A* **140**, 1133 (1965).

32. G. L. Goodman, D. E. Ellis, E. E. Alp, and L. Soderholm, Charge distributions and valency in copper oxide crystals related to superconductivity, *J. Chem. Phys.* **91**, 2983 (1989).
33. G. te Velde, ADF (Amsterdam Density Functional) user's guide, Department of Theoretical Chemistry, Vrije Universiteit Amsterdam.
34. B. Delley and D. E. Ellis, Efficient and accurate expansion methods for molecules in local density models, *J. Chem. Phys.* **4**, 76 (1982).
35. D. E. Ellis, G. A. Benesh, and E. Byrom, Molecular cluster studies of binary alloys: LiAl, *Phys. Rev. B* **16**, 3308 (1977).
36. P. Cortona, Self-consistently determined properties of solids without band-structure calculations, *Phys. Rev. B* **44**, 8454 (1991).
37. P. Cortona, Direct determination of self-consistent total energies and charge densities of solids: A study of the cohesive properties of the alkali halides, *Phys. Rev. B* **46**, 2008 (1992).
38. T. A. Wesolowski and A. Warshel, Frozen density functional approach for ab initio calculations of solvated molecules, *J. Phys. Chem.* **97**, 8050 (1993).
39. Following a referees comment with reference to our choice of Cortona's $V_{TF,nadd}$ potential in Eq. (12) to model orthogonality effects between fragment and surrounding density, we note that we have not investigated whether there is an advantage in using this particular functional form in contrast to other proposed forms (e.g., as discussed in [38]), including, as in Yang's formulations of D&C, a complete omission of such a potential.
40. B. I. Dunlap, J. W. Conolly, and J. R. Sabin, On some approximations in applications of $X\alpha$ theory, *J. Chem. Phys.* **71**, 3396 (1979).
41. J. Andzelm and E. Wimmer, Density functional Gaussian-type-orbital approach to molecular geometries, vibrations and reaction energies, *J. Chem. Phys.* **96**, 1280 (1992).
42. P. Pulay, Convergence acceleration of iterative sequences. The case of SCF iteration, *Chem. Phys. Lett.* **73**, 393 (1980).
43. P. Pulay, Improved SCF-convergence acceleration, *J. Comp. Chem.* **3**, 556 (1982).
44. J. Terra and D. E. Ellis, Electronic structure, chemical bonding and hyperfine parameters in layered silicates, *Phys. Rev. B* **56**, 1834 (1997).
45. H. Sticht, G. Wildegger, D. Bentrop, B. Darimont, R. Sterner, and P. Rösch, An NMR-derived model for the solution structure of oxidized thermotoga-maritima 1 [Fe_4S_4] ferredoxin, *Eur. J. Biochem.* **237**, 726 (1996).